Journal of Computational Physics 227 (2008) 8568–8587

Contents lists available at ScienceDirect

Journal of Computational Physics

journal homepage: www.elsevier.com/locate/jcp

SPH simulations of swimming linked bodies

J. Kajtar, J.J. Monaghan *

School of Mathematical Sciences, Monash University, Wellington Road, Clayton, Vic 3800, Australia

ARTICLE INFO

Article history:
Received 16 August 2007
Received in revised form 10 March 2008
Accepted 12 June 2008
Available online 19 June 2008

Keywords:
SPH
Swimming
Linked bodies
Navier–Stokes equations

ABSTRACT

In this paper, we describe how the swimming of linked-rigid bodies can be simulated using smoothed particle hydrodynamics (SPH). The fluid is assumed to be viscous and weakly compressible though with a speed of sound which ensures the Mach number is ~0.1 and the density fluctuation (relative to the average density) is typically 0.01. The motion is assumed to be two-dimensional. The boundaries of the rigid bodies are replaced by boundary particles and the forces between these particles and the fluid particles determine the forces and torques on the rigid bodies. The links between the bodies are described by constraint equations which are taken into account by Lagrange multipliers. We integrate the equations by a second-order method which conserves linear momentum exactly and, in the absence of viscosity, is reversible. We test our method by simulating the motion of a cylinder moving in a viscous fluid both under forced oscillation, and when tethered to a spring. We then apply our method to three problems involving three linked bodies. The first of these consists of three linked diamonds in a periodic domain and shows the convergence of the algorithm. The second is the system considered by Kanso et al. [E. Kanso, J.E. Marsden, C.W. Rowley, J.B. Melli-Huber, Locomotion of articulated bodies in a perfect fluid, J. Nonlinear Sci. 15 (2005) 255–289 (referred to in the text as K05)] and our results show similar behaviour for the same gait. The third example clarifies the conservation of angular momentum by simulating the motion of three linked ellipses moving within and through the surface of an initially circular patch of fluid. Our method can be easily extended to linked bodies swimming near surfaces, or to swimming near fixed boundaries of arbitrary shape, or to swimming in fluids which are stratified. Some of these systems have biological significance and others are applicable to the study of undersea vessels which move because of shape changes.

Crown Copyright © 2008 Published by Elsevier Inc. All rights reserved.

1. Introduction

This paper is concerned with the swimming of linked rigid bodies in an weakly compressible, viscous fluid. It is closely connected with mathematical and computational studies of the swimming of fish, and with the motion of underwater vehicles and robotic fish propelled by changes of shape. There is an extensive literature on observational studies of swimming fish beginning with the work of Gray [9], together with approximate analytical models for low Reynolds number swimming [11,18,34,36] and high Reynolds number swimming [17], Lighthill collected papers [19], and a monograph [3]. Reviews of fish swimming modes by Sfakiotakis et al. [35] and Triantafyllou et al. [37] discuss many experimental and mathematical studies of swimming in nature.

By comparison with the observational work on swimming, the numerical simulation of swimming is in its infancy. The early numerical work concentrated on highly simplified models, a typical example of which is the simulation of an oscillating

* Corresponding author.
E-mail address: joe.monaghan@sci.monash.edu.au (J.J. Monaghan).

0021-9991/$ - see front matter Crown Copyright © 2008 Published by Elsevier Inc. All rights reserved.
doi:10.1016/j.jcp.2008.06.004

filament [7] where the oscillation of the filament is specified as a simple wave and the motion is assumed to be forward. A common practice is to take details of the fish motion from observation and then use this information as a boundary condition on the flow. Wolfgang et al. [40] use this method to determine the near flow dynamics, especially the vorticity distribution, of a swimming giant danio. Liu et al. (1996, 1997) [20,21] calculated the flow induced by specified motion of a tadpole, but they did not calculate the full dynamics of tadpole and fluid. Attempts to model the complete motion of the fish and the fluid have not been so successful. For example, Carling et al. [1] simulated eel-like (aguiliform) motion, by solving the Navier–Stokes equations and including feedback from the fluid motion to that of the eel, but the resulting flow pattern disagrees with observations [38]. Both the analytical and numerical simulations have concentrated on forward motion rather than attempt the more complex turns and rapid accelerations of real fish.

The present simulations are closest to the recent work on the motion of linked bodies in a infinite, two-dimensional, inviscid (Kanso et al. (2005 subsequently referred to as K05) [12] and Melli et al. [22]) or viscous [5,6] fluid. When the fluid is inviscid it is possible to bring powerful mathematical formalisms to bear on the problem in a manner similar to the motion of a single body in an inviscid fluid (see for example [14]). However, for problems involving free surfaces, or complicated rigid boundaries, or a stratified fluid, these methods become very complicated.

The aim of this paper is to construct and test algorithms that can be used to study the swimming of linked bodies in configurations involving any combination of confined regions, free surfaces or stratified fluids. We use smoothed particle hydrodynamics (SPH) the details of which are described in a recent review [29] because it is easy to use for these complicated problems and, as we show here, the method gives satisfactory accuracy for moderate numbers of particles (defined as allowing us to run a simulation in 30 min on a Mac Powerbook). We take into account the viscous and pressure interaction between the bodies and the fluid by using boundary particles in a way which is similar to the immersed boundary method [32,33]. We show that these forces conserve linear and angular momentum, but the algorithm does not conserve angular momentum exactly because the conservation of angular momentum requires the constraints to be satisfied at the end of a time step whereas, in our algorithm, the constraints are satisfied at the mid-point of the time step. In the absence of viscosity, the numerical algorithm is reversible.

The plan of this paper is to first describe the SPH equations then the time stepping algorithm. We then test the algorithm by applying it to a number of test cases. The first of these is the calculation of the drag forces on a cylinder forced to move with simple harmonic motion in a stationary fluid. The experimental and the numerical results of other authors enable us to determine how the accuracy depends on the placement of boundary force particles on the boundary of the cylinder. The second test is the motion of a cylinder tethered to a spring and submerged in a viscous fluid. We show that the Strouhal number and the oscillation of the cylinder are in agreement with other calculations. We then consider a series of problems involving three linked bodies. These problems involve bodies with the shape of diamonds or ellipses, and the boundary conditions are either periodic or involve motion through a free surface.

2. Equations of motion and constraints

2.1. Equations of motion

We consider motion in two dimensions and use cartesian coordinates. A typical configuration of the bodies is shown in Fig. 1. The motion of the fluid, which is assumed incompressible, is specified by the Navier–Stokes equations. In cartesian tensor form these equations are

$$\frac{dv_i}{dt} = \frac{1}{\rho}\frac{\partial \sigma_{ij}}{\partial x^j} + \frac{1}{\rho}\sum_{k=1}^{N_b} \sigma_{ij} n_j(k)\delta(s_k), \tag{2.1}$$

where σ_{ij} is the stress tensor

$$\sigma_{ij} = -P\delta_{ij} + \mu\left(\frac{\partial v_i}{\partial x_j} + \frac{\partial v_j}{\partial x_i} - \frac{2}{3}\delta_{ij}\frac{\partial v_\ell}{\partial x_\ell}\right). \tag{2.2}$$

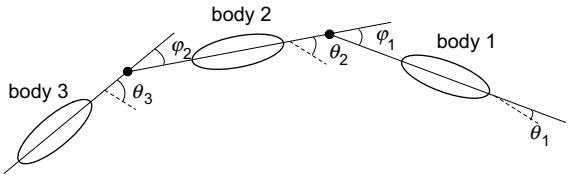

Fig. 1. The configuration of the bodies (assumed to be ellipses). The link position is denoted by a filled circle. The straight line through a body passes through its centre of mass and is assumed to be rigidly attached to the body with one end attached to the link. The angles θ are defined relative to a fixed direction in space (shown by parallel dotted lines) which is taken to be the x-axis of a cartesian coordinate system in our calculations. The angles φ determine the gait and are specified functions of the time.

P is the pressure and μ is the viscosity coefficient. The function $\delta(s_k)$ is a one-dimensional delta function, and s_k is the perpendicular distance from the surface A_k of body k to the position where the fluid acceleration is required. The unit vector $n_j(k)$ is directed from body k into the fluid. If (2.1) is integrated over a small volume enclosing part of one of the bodies, the term involving the delta function gives the reaction force of that body on the fluid. This formulation is similar to that of Peskin [32].

An element of area on the surface of body k is denoted by $\mathrm{d}A(k)$. The motion of the centre of mass $\mathbf{R}(k)$ of solid body k (with mass $M(k)$) is given by

$$M(k)\frac{\mathrm{d}^2R^i(k)}{\mathrm{d}t^2} = -\int \sigma^{ij}n^j(k)\mathrm{d}A(k) + F^i(k), \tag{2.3}$$

where $\mathbf{F}(k)$ is the force due to the constraints. The rotation of rigid body k (with moment of inertia $I(k)$) is given by

$$I(k)\frac{\mathrm{d}^2\theta_k}{\mathrm{d}t^2} = \int (\mathbf{d}_k \times \mathbf{b})\mathrm{d}A(k) + \tau(k), \tag{2.4}$$

where $\mathbf{d}_k$ is a vector from the centre of mass of body k to the element of area $\mathrm{d}A_k$, $\mathbf{b}$ is the force on the element of area, and $\tau(k)$ is the constraint torque on body k.

In the following, to simplify the notation, the subscript k will always denote the label of a body. Thus, for example, $\mathbf{R}(k)$ will be replaced by $\mathbf{R}_k$.

2.2. Constraint equations forces and torques

The angle θ_k which fixes the rotation of body k is defined as the positive rotation of a line fixed in the body from the x-axis of a cartesian coordinate system fixed in space. For simplicity we assume the line fixed in the body is an axis of symmetry. The constraint conditions on the angles are

$$\varphi_m = \theta_{m+1} - \theta_m, \tag{2.5}$$

where m is the link number and φ_m is a specified function. The form of the φ_m determines the gait of the bodies. For the examples we consider here there are three bodies and two links as shown in Fig. 1. In the simplest case φ_m is a function of t but, in general, it depends on other variables. For example, in a biological problem, it could depend on the centre of mass coordinates in such a way that the fish slows down when it enters a region where the food supply is rich. As an example φ_1 could be given by $\cos(tX_1^2)$, so that the frequency of the motion is spatially dependent.

In addition to the constraints on the angles there are constraints associated with the links. We assume the link, or pivot, is at a distance ℓ_k from the centre of mass of body k. The condition on the X components of the centres of mass of bodies k and $k+1$ is that the X coordinate of the link between them is given by

$$X_k - \ell_k\cos(\theta_k) = X_{k+1} + \ell_{k+1}\cos(\theta_{k+1}), \tag{2.6}$$

or

$$X_k - \ell_k\cos(\theta_k) - X_{k+1} - \ell_{k+1}\cos(\theta_{k+1}) = 0. \tag{2.7}$$

Similarly the Y constraint is

$$Y_k - \ell_k\sin(\theta_k) - Y_{k+1} - \ell_{k+1}\sin(\theta_{k+1}) = 0. \tag{2.8}$$

These constraints enable the coordinates of the centres of mass of the bodies, and their angles θ to be written in terms of those of any selected body. Similarly, by differentiating the constraint conditions with respect to time, the velocities $\dot{X}$ and $\dot{Y}$ and angular velocity Ω of the bodies can be written as functions of the same selected body. The number of degrees of freedom (coordinates and velocities) of N linked bodies in two dimensions is therefore 6 compared with the $6N$ degrees of freedom of N independent bodies in two dimensions. If the φ_m are functions of t alone it is possible to reduce the equations of motion to those involving the coordinates and velocities of one of the bodies. However, when the φ_m are functions of both coordinates and time, as in the example above, it is inconvenient to eliminate variables. Because we wish to develop an algorithm which can be used in these more general cases we take account of the constraints by Lagrange multipliers even though, in the applications to be described in this paper, the φ_m are functions of t.

For the case of three bodies we have two links and therefore 6 constraints. We denote the Lagrange multipliers for the X, Y and θ constraints of link m by $\Lambda_X^{(m)}$, $\Lambda_Y^{(m)}$ and $\Lambda_\theta^{(m)}$, respectively. Using standard methods for holonomic constraints (e.g. [15]) we find the following expressions for the constraint forces $\mathbf{F}_k$ and torques τ_k for the various bodies. For body 1

$$\mathbf{F}_1 = (\lambda_X^{(1)}, \lambda_Y^{(1)}), \tag{2.9}$$

for body 2

$$\mathbf{F}_2 = (-\lambda_X^{(1)}, -\lambda_Y^{(1)}) + (\lambda_X^{(2)}, \lambda_Y^{(2)}) \tag{2.10}$$

and for body 3

$$\mathbf{F}_3 = (-\lambda_X^{(2)}, -\lambda_Y^{(2)}). \tag{2.11}$$

These constraint forces do not affect the total linear momentum of the bodies because they sum to zero.

The constraint torque on body 1 is

$$\tau_1 = -\lambda_\theta^{(1)} + \lambda_X^{(1)}\ell_1 \sin(\theta_1) - \lambda_Y^{(1)}\ell_1 \cos(\theta_1), \tag{2.12}$$

on body 2 it is

$$\tau_2 = \lambda_\theta^{(1)} - \lambda_\theta^{(2)} + \lambda_X^{(1)} + \lambda_X^{(2)}\ell_2 \sin(\theta_2) - (\lambda_Y^{(1)} + \lambda_Y^{(2)})\ell_2 \cos(\theta_2) \tag{2.13}$$

and on body 3 it is

$$\tau_3 = \lambda_\theta^{(2)} + \lambda_X^{(2)}\ell_3 \sin(\theta_3) - \lambda_Y^{(2)}\ell_3 \cos(\theta_3). \tag{2.14}$$

The way these constraint forces and torques affect the angular momentum will be discussed in Sections 5 and 6.

3. SPH equations for the fluid

The form of the SPH equations that we use is discussed in more detail by Monaghan [23,29]. For the liquid SPH particles the acceleration equation is

$$\frac{\mathrm{d}\mathbf{v}_a}{\mathrm{d}t} = -\sum_b m_b \left(\frac{P_a}{\rho_a^2} + \frac{P_b}{\rho_b^2} + \Pi_{ab} + R_{ab}\right)\nabla_a W_{ab} + \sum_{k=1}^{N_b}\sum_{j\in S_k}[\mathbf{f}_{aj} - m_j \Pi_{aj}\nabla_a W_{aj}]. \tag{3.1}$$

In this equation the mass, position, velocity, density and pressure of particle a are m_a, $\mathbf{r}_a$, $\mathbf{v}_a$, ρ_a and P_a, respectively. W_{ab} denotes the smoothing kernel $W(\mathbf{r}_a - \mathbf{r}_b, \bar{h}_{ab})$ and ∇_a denotes the gradient taken with respect to the coordinates of particle a. In this paper, W is the cubic spline kernel [29], and has support $2\bar{h}_{ab}$. In the present calculations the $\bar{h}_{ab}$ used in W_{ab} is an average $\bar{h}_{ab} = (h_a + h_b)/2$. The choice of h is discussed in detail by Monaghan [23,29]. We choose h to be 1.3 times the initial particle spacing so that the interaction between any two fluid particles is zero beyond 2.6 initial particle spacings.

The first summation in (3.1) is over all fluid particles and is the SPH equivalent of the first term on the right-hand side of (2.1). The last term in (3.1) is the contribution to the force per unit mass on fluid particle a due to boundary particles. k denotes a body label, and $j \in S_k$ is one of the set of boundary particle label on body k. The term $\mathbf{f}_{aj}$ is a non-viscous boundary particle force per unit mass (see below). The viscosity is determined by Π_{ab} for which we choose the form [25,29]

$$\Pi_{ab} = -\frac{\alpha v_{\mathrm{sig}} \mathbf{v}_{ab}\cdot\mathbf{r}_{ab}}{\rho_{ab}|\mathbf{r}_{ab}|}. \tag{3.2}$$

In this expression α is a constant, and the notation $\mathbf{v}_{ab} = \mathbf{v}_a - \mathbf{v}_b$ is used. ρ_{ab} denotes the average density $\frac{1}{2}(\rho_a + \rho_b)$. We take the signal velocity to be

$$v_{\mathrm{sig}} = \frac{1}{2}(c_a + c_b) - 2\frac{\mathbf{v}_{ab}\cdot\mathbf{r}_{ab}}{r_{ab}}, \tag{3.3}$$

where c_a is the speed of sound at particle a ([25] though here we take v_{sig} to be half used in that paper and α is therefore a factor 2 larger). The kinematic viscosity can be estimated by taking the continuum limit which is equivalent to letting the number of particles go to infinity while keeping the resolution length h constant. By a calculation similar to that in Monaghan [29] it is found that the kinematic viscosity is given by

$$\nu = \frac{15}{112}\alpha h v_{\mathrm{sig}}. \tag{3.4}$$

SPH calculations for shear flow agree very closely with theoretical results using this kinematic viscosity [30].

The pressure is given by

$$P_a = \frac{\rho_0 c_a^2}{7}\left(\left(\frac{\rho_a}{\rho_0}\right)^7 - 1\right), \tag{3.5}$$

where ρ_0 is the reference density of the fluid. To ensure the flow has a sufficiently low Mach number to approximate a constant density fluid accurately, we determine the speed of sound by $c_a \sim 10V$ where V is the maximum speed of the fluid relative to the bodies. In this case v_{sig} is dominated by the first two terms. The precise value of c_a will be specified for each simulation.

The term R_{ab} is an anti-clumping term [10,26] which acts to prevent SPH particles clustering in pairs during a simulation. It is primarily needed for simulations when the pressure becomes negative or, more generally, the material is in tension. For the present simulations R_{ab} is given by

$$R_{ab} = 0.01\left|\frac{P_a}{\rho_a^2} + \frac{P_b}{\rho_b^2}\right|\left(\frac{W_{ab}}{W(\Delta p)}\right)^4, \tag{3.6}$$

where $W(\Delta p)$ is the kernel evaluated at an initial particle spacing Δp. Because the coefficient is small, and W falls off rapidly with the particle separation, this term reduces the clustering of SPH particles without significantly affecting the motion on the scale of several particle separations.

The form of the SPH continuity equation we use here is

$$\frac{\mathrm{d}\rho_a}{\mathrm{d}t} = \sum_b m_b \mathbf{v}_{ab} \cdot \nabla W_{ab} \tag{3.7}$$

and the position of any fluid particle a is found by integrating

$$\frac{\mathrm{d}\mathbf{r}_a}{\mathrm{d}t} = \mathbf{v}_a. \tag{3.8}$$

In the present simulations the liquid SPH particles were initially placed on a grid of squares and thereafter allowed to move in response to the forces. The surfaces of the bodies are defined by a set of particles called boundary particles. These particles exert forces on the fluid and in turn experience forces. The sum of the forces on the boundary particles of a body gives the force on that body due to the fluid, and the forces determine the torque about the centre of mass of the body. This method of treating surfaces [24] is similar to the immersed boundary method of Peskin [32,33].

In the present simulations we use the improved treatment of the boundary forces described by Monaghan et al. [28] with the addition of a small correction to ensure the boundary forces conserve angular momentum. These forces are such that the force per unit mass on liquid particle a due to boundary particle j is

$$\mathbf{f}_{aj} = \frac{m_j}{m_a + m_j} N(y'_{aj}) T(x'_{aj}) \mathbf{n}_j, \tag{3.9}$$

where $\mathbf{n}_j$ is the unit normal at particle j. The function N is an approximation to the delta function and y'_{aj} is measured perpendicular to the surface. The function $T(x'_{aj})$, where x'_{aj} is measured tangential to the surface, is an interpolating function which ensures that particle a can only interact with at most two boundary particles, and the force on particle a is constant as it moves between a pair of boundary particles. The force per unit mass on boundary particle j due to liquid particle a is

$$\mathbf{f}_{ja} = -\frac{m_a}{m_a + m_j} N(y'_{aj}) T(x'_{aj}) \mathbf{n}_j, \tag{3.10}$$

so that the force on particle j, namely $m_j \mathbf{f}_{ja}$, and that on particle a, namely $m_a \mathbf{f}_{aj}$, are equal and opposite. In the paper of Monaghan et al. [28], the function $N(y')$ vanishes for $y' > 2h$. Our correction is that $N(y')$ vanishes if $y' > 2h^*$ where

$$h^* = \sqrt{h^2 - \frac{1}{4}\Delta p^2} \tag{3.11}$$

and Δp is the boundary particle spacing. By restricting the range in this way we ensure that when a fluid particle has a non-zero interaction with boundary particles, it is always with a pair of boundary particles and this guarantees that angular momentum will be conserved by the boundary forces. The previous discussion applies to convex bodies. If a section of the surface is concave we do not know of any entirely satisfactory way of using normals. The bodies considered in this paper have convex surfaces.

4. SPH equations for the rigid bodies

The non-viscous force on boundary particle j due to all fluid particles is

$$\mathbf{f}_j^{(nv)} = m_j \sum_a \mathbf{f}_{ja}, \tag{4.1}$$

and the viscous force is

$$\mathbf{f}_j^{(v)} = -m_j \sum_a m_a \Pi_{aj} \nabla_j W_{aj} = m_j \sum_a m_a \Pi_{aj} \nabla_a W_{aj}, \tag{4.2}$$

where we have used the fact that $\nabla_j W_{aj} = -\nabla_a W_{aj}$. The total force on particle j is

$$\mathbf{f}_j = \mathbf{f}_j^{(nv)} + \mathbf{f}_j^{(v)}. \tag{4.3}$$

The equation for the centre of mass motion of body k is then

$$M_k \frac{\mathrm{d}\mathbf{V}_k}{\mathrm{d}t} = \sum_{j \in S_k} \mathbf{f}_j + \mathbf{F}_k \tag{4.4}$$

and the torque equation is

$$I_k \frac{\mathrm{d}\Omega_k}{\mathrm{d}t} = \sum_{j\in S_k} (\mathbf{r}_j - \mathbf{R}_k) \times \mathbf{f}_j + \tau_k. \tag{4.5}$$

The motion of a boundary particle can be determined from the motion of centre of mass and the rotation about the centre of mass. Thus for particle j on body k,

$$\frac{\mathrm{d}\mathbf{r}_j}{\mathrm{d}t} = \mathbf{V}_k + \Omega_k \hat{\mathbf{z}} \times (\mathbf{r}_j - \mathbf{R}_k), \tag{4.6}$$

where in this two-dimensional problem, the rotation is around the z axis which is perpendicular to the plane of the motion. The equation of motion of the unit normals on the boundary can be calculated from

$$\frac{\mathrm{d}\mathbf{n}_j}{\mathrm{d}t} = \Omega_k \hat{\mathbf{z}} \times \mathbf{n}_j, \tag{4.7}$$

or they can be calculated from the coordinates of its neighbouring boundary particles.

5. Conservation of linear and angular momentum

The total rate of change of the linear momentum of the rigid bodies with respect to time is

$$\sum_k M_k \frac{\mathrm{d}\mathbf{V}_k}{\mathrm{d}t} = \sum_k \sum_{j\in S_k} \mathbf{f}_j = \sum_k \sum_{j\in S_k} \sum_a m_j [\mathbf{f}_{ja} - m_a \nabla_j W_{aj}], \tag{5.1}$$

where as noted earlier, the sum over the constraint forces is zero. The rate of change of linear momentum of the fluid SPH particles is given by

$$\sum_a m_a \frac{\mathrm{d}\mathbf{v}_a}{\mathrm{d}t} = \sum_a \sum_k \sum_{j\in S_k} m_a [\mathbf{f}_{aj} - m_j \Pi_{aj} \nabla_a W_{aj}], \tag{5.2}$$

noting that the sum over the pressure, anti-clumping and viscous forces between fluid particles vanishes because of symmetry.

Recalling that

$$\sum_a m_j \mathbf{f}_{ja} = -\sum_a m_a \mathbf{f}_{aj} \text{ and } \nabla_a W_{aj} = -\nabla_j W_{aj}, \tag{5.3}$$

we deduce that

$$\sum_k M_k \frac{\mathrm{d}\mathbf{V}_k}{\mathrm{d}t} + \sum_a m_a \frac{\mathrm{d}\mathbf{v}_a}{\mathrm{d}t} = 0, \tag{5.4}$$

which shows that the linear momentum

$$\sum_k M_k \mathbf{V}_k + \sum_a m_a \mathbf{v}_a \tag{5.5}$$

is conserved.

The angular momentum of the bodies is composed of the centre of mass angular momentum about some fixed origin, and the sum over each body of the spin angular momentum about the centre of mass of body. The time rate of change of the total centre of mass angular momentum is

$$\sum_k M_k \mathbf{R}_k \times \frac{\mathrm{d}\mathbf{V}_k}{\mathrm{d}t} = \sum_k \mathbf{R}_k \times \sum_{j\in S_k} \mathbf{f}_j + \sum_k \mathbf{R}_k \times \mathbf{F}_k, \tag{5.6}$$

the rate of change of the spin angular momentum is

$$\sum_k I_k \frac{\mathrm{d}\Omega}{\mathrm{d}t} = \sum_k \sum_{j\in S_k} (\mathbf{r}_j - \mathbf{R}_k) \times \mathbf{f}_j + \sum_k \tau_k. \tag{5.7}$$

The rate of change of the angular momentum of the fluid particles is

$$\sum_a m_a \mathbf{r}_a \times \frac{\mathrm{d}\mathbf{v}_a}{\mathrm{d}t} = \sum_a \sum_k \sum_{j\in S_k} m_a \mathbf{r}_a \times [\mathbf{f}_{aj} - m_j \Pi_{aj} \nabla_a W_{aj}], \tag{5.8}$$

where because of symmetry, the sum over pressure, viscous and anti-clumping terms between fluid particles have vanished. The rate of change of the total angular momentum (the sum of (5.6)–(5.8)) becomes

$$\frac{dJ}{dt} = \sum_a \sum_k \sum_{j\in S_k} m_a(\mathbf{r}_j - \mathbf{r}_a)\times \mathbf{f}_{aj}, + \lambda_X^{(1)}(-Y_1 + \ell_1\sin(\theta_1) + Y_2 + \ell_2\sin(\theta_2)) + \lambda_Y^{(1)}(X_1 - \ell_1\cos(\theta_1) - X_2 - \ell_2\cos(\theta_2)) + \lambda_X^{(2)}(-Y_2 + \ell_2\sin(\theta_2) + Y_3 + \ell_3\sin(\theta_3)) + \lambda_Y^{(2)}(X_2 - \ell_2\cos(\theta_2) + X_3 - \ell_3\cos(\theta_3)). \tag{5.9}$$

The last four terms vanish because of the constraint conditions (2.7) and (2.8). The remaining term involves the boundary forces and it can be shown that this term vanishes [29].

Finally, we note that the previous arguments about conservation assume the time derivatives are exact. The actual conservation in the numerical simulations depends on the form of the time stepping algorithm. Anticipating results from the next section, we find that linear momentum is always conserved to round off error, but the angular momentum conservation is less accurate because the Lagrange multipliers are calculated at the mid-point. In some of the simulations we use periodic and these do not conserve angular momentum exactly.

5.1. Remarks concerning external boundaries

The SPH equations can be applied to the linked bodies moving in a channel, as is the case for many laboratory experiments on fish, or in a pond with an irregular boundary, by replacing the boundaries of the pond by boundary force particles as we have done for the rigid bodies. We employ this method in our second test case. The SPH algorithm does not need to be changed if the linked bodies move through and out of a free surface, which is required to mimic the motion of dolphins. This facility was used earlier for bodies hitting the water [27,28] and we illustrate it here in an example involving three linked bodies. If the swimming occurs in a flowing stream, SPH fluid particles can be injected with the appropriate speed and density as in the tethered cylinder simulation described below. A convenient alternative is to superpose the stream velocity on the body, and set the upstream velocity to zero.

In the present paper, where we compare our results with those of Kanso et al. [12], we need to deal with an infinite medium. This cannot be done directly because it would require infinitely many particles. One alternative, and the simplest, is to replace fluids of infinite extent by periodic boundary conditions. These boundaries alter the solutions of the differential equations but the effects are small if the periodic cells are sufficiently large. The periodic boundaries do not affect the conservation of linear momentum but they do affect the conservation of angular momentum because two particles that do not interact directly may interact with their images. To test this (Section 8.2.3) we simulated a fluid in an axisymmetric potential well and allowed the linked bodies to swim through the surface. The conservation was a factor $\sim$1000 better than with the periodic cells. It was not accurate to round off because, as noted earlier, the constraints are only satisfied to round off accuracy at the end of the step, whereas the conservation depends on how accurately the constraints are satisfied at the mid-point of the steps.

6. Time stepping

The SPH equations were integrated using a second-order scheme based on the symplectic Verlet integrator. The system conserves linear momentum exactly (to round off), and is reversible when the viscosity is zero. The errors in the angular momentum conservation due to the periodic boundaries and the constraints have been discussed earlier.

There are two stages to the integration. In the first stage the mid-point quantities are calculated, and in the second, after the various forces have been obtained, the step is completed. Throughout this section, for any quantity $\mathbf{A}$, $\mathbf{A}^0$ denotes its value at the beginning of the time step, $\mathbf{A}^{1/2}$ at the mid-point, and $\mathbf{A}^1$ at the end of the step.

To simplify the expressions for the time stepping we write the SPH fluid equations in the form

$$\frac{d\mathbf{r}_a}{dt} = \mathbf{v}_a, \tag{6.1}$$

$$\frac{d\mathbf{v}_a}{dt} = \mathscr{F}_a, \tag{6.2}$$

$$\frac{d\rho_a}{dt} = D_a, \tag{6.3}$$

where

$$\mathscr{F}_a = -\sum_b m_b\left(\frac{P_a}{\rho_a^2} + \frac{P_b}{\rho_b^2} + \Pi_{ab} + R_{ab}\right)\nabla_a W_{ab} + \sum_{k=1}^{n_b}\sum_{j\in S_k}[\mathbf{f}_{aj} - m_j\Pi_{aj}\nabla_a W_{aj}], \tag{6.4}$$

$$D_a = \sum_b m_b \mathbf{v}_{ab}\cdot\nabla W_{ab}. \tag{6.5}$$

In the first stage of the integration, the mid-point values are calculated for $\mathbf{r}_a$, ρ_a and h_a, the body positions and orientations $\mathbf{R}_k$, θ_k, and the relative boundary particle positions $\mathbf{d}_j = \mathbf{r}_j - \mathbf{R}_k$, and their normals $\hat{\mathbf{n}}_j$. With δt denoting the time step

$$\mathbf{r}_a^{1/2} = \mathbf{r}_a^0 + \frac{1}{2}\delta t\mathbf{v}_a^0, \tag{6.6}$$

$$\rho_a^{1/2} = \rho_a^0 + \frac{1}{2}\delta t D_a^0, \tag{6.7}$$

$$h_a^{1/2} = h_a^0\left(1 - \frac{1}{4}\delta t D_a^0/\rho_a^0\right), \tag{6.8}$$

$$\mathbf{R}_k^{1/2} = \mathbf{R}_k^0 + \frac{1}{2}\delta t \mathbf{V}_k^0, \tag{6.9}$$

$$\theta_k^{1/2} = \theta_k^0 + \frac{1}{2}\delta t \Omega_k^0, \tag{6.10}$$

$$\mathbf{d}_j^{1/2} = \mathbf{d}_j^0 + \frac{1}{2}\delta t \Omega_k^0 \hat{\mathbf{z}} \times \mathbf{d}_j^0, \tag{6.11}$$

$$\mathbf{r}_j^{1/2} = \mathbf{d}_j^{1/2} + \mathbf{R}_k^{1/2}, \tag{6.12}$$

$$\hat{\mathbf{n}}_j^{1/2} = \hat{\mathbf{n}}_j^0 + \frac{1}{2}\delta t \Omega_k^0 \hat{\mathbf{z}} \times \hat{\mathbf{n}}_j^0. \tag{6.13}$$

With the mid-point coordinates known, $\mathscr{F}_a^{1/2}, \mathbf{f}_j^{1/2}, \mathbf{F}_k^{1/2}$ and $\tau_k^{1/2}$ can be calculated. The last two involve the Lagrange multipliers and their calculation is discussed later. The time-step for $\mathbf{v}$ and $\mathbf{r}$ is then completed by

$$\mathbf{v}_a^1 = \mathbf{v}_a^0 + \delta t \mathscr{F}_a^{1/2}, \tag{6.14}$$

$$\mathbf{r}_a^1 = \mathbf{r}_a^{1/2} + \frac{1}{2}\delta t \mathbf{v}_a^1. \tag{6.15}$$

With $\mathbf{v}^1$ and $\mathbf{r}^1$ known D_a^1 can be calculated (this requires another sweep over the particles) and the step for ρ and h completed according to

$$\rho_a^1 = \rho_a^{1/2} + \frac{1}{2}\delta t D_a^1, \tag{6.16}$$

$$h_a^1 = \frac{h_a^{1/2}}{1 + \frac{1}{4}\delta t\left(\frac{D_a^1}{\rho_a^1}\right)}. \tag{6.17}$$

The step for the body velocity, coordinates, angles and angular velocity is completed by

$$\mathbf{V}_k^1 = \mathbf{V}_k^0 + \frac{\delta t}{M_k}\left(\sum_{j\in S_k} \mathbf{f}_j^{1/2} + \mathbf{F}_k^{1/2}\right), \tag{6.18}$$

$$\mathbf{R}_k^1 = \mathbf{R}_k^{1/2} + \frac{1}{2}\delta t \mathbf{V}_k^1, \tag{6.19}$$

$$\Omega_k^1 = \Omega_k^0 + \frac{\delta t}{I_k}\left(\sum_{j\in S_k} \mathbf{d}_j^{1/2} \times \mathbf{f}_j^{1/2} + \tau_k^{1/2}\right), \tag{6.20}$$

$$\theta_k^1 = \theta_k^{1/2} + \frac{1}{2}\delta t \Omega_k^1 \tag{6.21}$$

and the positions and normals of the body boundary particles at the end of the step are given by

$$\mathbf{d}_j^1 = \frac{\mathbf{d}_j^{1/2} + \frac{1}{2}\delta t \Omega_k^1 \hat{\mathbf{z}} \times \mathbf{d}_j^{1/2}}{1 + \left(\frac{1}{2}\delta t \Omega_k^1\right)^2}, \tag{6.22}$$

$$\mathbf{r}_j^1 = \mathbf{d}_j^1 + \mathbf{R}_k^1, \tag{6.23}$$

$$\hat{\mathbf{n}}_j^1 = \frac{\hat{\mathbf{n}}_j^{1/2} + \frac{1}{2}\delta t \Omega_k^1 \hat{\mathbf{z}} \times \hat{\mathbf{n}}_j^{1/2}}{1 + (\frac{1}{2}\delta t \Omega_k^1)^2}. \tag{6.24}$$

The time stepping for $\mathbf{d}$ and $\mathbf{n}$ is identical, and is based on the fact that they both satisfy an equation of the form

$$\frac{\mathrm{d}\mathbf{q}}{\mathrm{d}t} = \boldsymbol{\Omega} \times \mathbf{q}, \tag{6.25}$$

which can be integrated reversibly according to

$$\mathbf{q}^{1/2} = \mathbf{q}^0 + \frac{1}{2}\delta t \boldsymbol{\Omega}^0 \times \mathbf{q}^0, \tag{6.26}$$

$$\mathbf{q}^1 = \mathbf{q}^{1/2} + \frac{1}{2}\delta t \boldsymbol{\Omega}^1 \times \mathbf{q}^1. \tag{6.27}$$

The last equation can be solved by taking the vector cross product with $\Omega_k^1 \hat{\mathbf{z}}$, and, on substituting the resulting expression for $\boldsymbol{\Omega}^1 \times \mathbf{q}^1$ into (6.27), gives

$$\mathbf{q}_j^1 = \frac{\mathbf{q}_j^{1/2} + \frac{1}{2}\delta t \Omega_k^1 \hat{\mathbf{z}} \times \mathbf{q}_j^{1/2}}{1 + \left(\frac{1}{2}\delta t \Omega_k^1\right)^2}. \tag{6.28}$$

It can be shown that if $|\mathbf{q}^0| = 1$, then $|\mathbf{q}^{1/2}| = 1 + \left(\frac{1}{2}\delta t \Omega^0\right)^2$. The mid-point value is therefore in error by terms of order $(\delta t)^2$ as are the other mid-point quantities. However, at the end of the step, the errors in $\mathbf{q}^1$ are of order $(\delta t)^3$. If desired the normals can be calculated from the positions of nearest neighbour boundary particles.

The time step, δt, is set from the Courant condition

$$\delta t^1 = 0.5 \times \min\left(\delta t^0, \frac{\bar{h}^{1/2}}{v_{\mathrm{sig}}^{1/2}}\right), \tag{6.29}$$

where the minimum is over all fluid particles (calculated when the forces are calculated) and the exponent convention is the same as for the time stepping. There are two further possible time step constraints. The first is from the boundary forces and this is discussed by Monaghan et al. [28] and implemented here. The second time step constraint is due to the constraint forces and torques. This time step control is based on the condition that, during a step, the change in position of the centre of mass of the bodies due to the force should be much less than h, with a similar condition for the change in position of any point on the surface of the bodies due to the torque. However, in our simulations, the Courant condition always requires a smaller time step than that from the constraint forces and torques.

It is easy to show that the time stepping equations conserve linear momentum. The change in the total angular momentum can be shown to result in a similar expression to (5.9). However, all the terms arising from the constraints are evaluated at the mid-point, whereas the Lagrange multipliers are determined by requiring the constraints to be satisfied at the end of the step. Because the constraints are not satisfied at the mid-point the rate of change of angular momentum will not be zero. Leimkuhler and Skeel [16] discuss how the constraint and its derivative (the latter is called a hidden constraint) can be calculated, but they find that the improvement in overall accuracy is negligible. In agreement with their result we also find that the error in the angular momentum is negligible.

7. The calculation of the lagrange multipliers

7.1. The equations

The Lagrange multipliers were determined by requiring that the constraints were satisfied at the end of each time-step. Because our results are easily generalised to an arbitrary number of links, we assume for simplicity that there are three bodies and therefore two links. The angle constraint at the first link requires

$$\varphi_1^1 = \theta_2^1 - \theta_1^1. \tag{7.1}$$

Substituting the time stepping rules for the final angles we get

$$\varphi_1^1 = \Phi_2 - \Phi_1 + \frac{(\delta t)^2}{2I_k}\left(\tau_2^{1/2} - \tau_1^{1/2}\right), \tag{7.2}$$

where

$$\Phi_k = \theta_k^{1/2} + \frac{\delta t}{2}\Omega_k^0 + \frac{(\delta t)^2}{2I_k}\sum_{j\in S_k} \mathbf{d}_j^{1/2} \times \mathbf{f}_j^{1/2}. \tag{7.3}$$

Note that Φ_k contains only quantities known from the first half step of our integration. After substituting the expressions for the constraint torques, and some minor rearrangement, the constraint condition (7.1) becomes, using the notation, $s_k = \sin(\theta_k^{1/2})$ and $c_k = \cos(\theta_k^{1/2})$,

$$G_\theta^{(1)} = 0 = -\frac{2\varphi_1^1}{(\delta t)^2} + \frac{2(\Phi_2 - \Phi_1)}{(\delta t)^2} + \lambda_\theta^{(1)}\left(\frac{1}{I_1} + \frac{1}{I_2}\right) - \lambda_\theta^{(2)}\frac{1}{I_2} + \lambda_X^{(1)}\left(\frac{\ell_2 s_2}{I_2} - \frac{\ell_1 s_1}{I_1}\right) + \lambda_Y^{(1)}\left(-\frac{\ell_2 c_2}{I_2} + \frac{\ell_1 c_1}{I_1}\right) + \lambda_X^{(2)}\frac{\ell_2 s_2}{I_2} - \lambda_Y^{(2)}\frac{\ell_2 c_2}{I_2} \tag{7.4}$$

and the angle constraint for the second link becomes

$$G_\theta^{(2)} = 0 = -\frac{2\varphi_2^1}{(\delta t)^2} + \frac{2(\Phi_3 - \Phi_2)}{(\delta t)^2} - \lambda_\theta^{(1)}\frac{1}{I_2} + \lambda_\theta^{(2)}\left(\frac{1}{I_2} + \frac{1}{I_3}\right) - \lambda_X^{(1)}\frac{\ell_2 s_2}{I_2} + \lambda_Y^{(1)}\frac{\ell_2 c_2}{I_2} + \lambda_X^{(2)}\left(\frac{\ell_3 s_3}{I_3} - \frac{\ell_2 s_2}{I_2}\right) + \lambda_Y^{(2)}\left(-\frac{\ell_3 c_3}{I_3} + \frac{\ell_2 c_2}{I_2}\right). \tag{7.5}$$

These equations are linear in the Lagrange multipliers.

Similarly, the constraints on the X and Y coordinates for the first link, must be satisfied at the end of the step. The constraint equation for the X coordinates at link 1 can be written

$$G_X^{(1)} = 0 = \frac{2(\Psi_{X_1} - \Psi_{X_2})}{(\delta t)^2} + \lambda_X^{(1)}\left(\frac{1}{M_1} + \frac{1}{M_2}\right) - \lambda_X^{(2)}\frac{1}{M_2} - \frac{2}{(\delta t)^2}\left(\ell_1 \cos(\theta_1^1) + \ell_2 \cos(\theta_2^1)\right), \tag{7.6}$$

where Ψ_{X_k} and Ψ_{Y_k} are the X and Y components of

$$\mathbf{\Psi}_k = \mathbf{R}_k^{1/2} + \frac{\delta t}{2}\mathbf{V}_k^0 + \frac{(\delta t)^2}{2M_k}\sum_{j\in S_k}\mathbf{f}_j^{1/2}. \tag{7.7}$$

This constraint equation is non-linear in the Lagrange multipliers because the numerical algorithm involves trignometric functions of the angles at the end of the step, and these contain Lagrange multipliers. Thus from (6.20) and (6.21), (2.12), (2.13) and (2.14),

$$\theta_1^1 = \Phi_1 + \frac{(\delta t)^2}{2I_1}(-\lambda_\theta^{(1)} + \lambda_X^{(1)}\ell_1 s_1 - \lambda_Y^{(1)}\ell_1 c_1), \tag{7.8}$$

$$\theta_2^1 = \Phi_2 + \frac{(\delta t)^2}{2I_2}(\lambda_\theta^{(1)} - \lambda_\theta^{(2)} + \lambda_X^{(1)}\ell_2 s_2 - \lambda_Y^{(1)}\ell_2 c_2 + \lambda_X^{(2)}\ell_2 s_2 - \lambda_Y^{(2)}\ell_2 c_2), \tag{7.9}$$

$$\theta_3^1 = \Phi_3 + \frac{(\delta t)^2}{2I_3}(\lambda_\theta^{(2)} + \lambda_X^{(2)}\ell_3 s_3 - \lambda_Y^{(2)}\ell_3 c_3). \tag{7.10}$$

The Y coordinate constraint for link 1 is

$$G_Y^{(1)} = 0 = \frac{2(\Psi_{Y_1} - \Psi_{Y_2})}{(\delta t)^2} + \lambda_Y^{(1)}\left(\frac{1}{M_1} + \frac{1}{M_2}\right) - \lambda_Y^{(2)}\frac{1}{M_2} - \frac{2}{(\delta t)^2}\left(\ell_1 \sin(\theta_1^1) + \ell_2 \sin(\theta_2^1)\right). \tag{7.11}$$

The X, Y coordinate constraints for the second link have the same pattern. They are

$$G_X^{(2)} = 0 = \frac{2(\Psi_{X_2} - \Psi_{X_3})}{(\delta t)^2} - \lambda_X^{(1)}\frac{1}{M_2} + \lambda_X^{(2)}\left(\frac{1}{M_2} + \frac{1}{M_3}\right) - \frac{2}{(\delta t)^2}\left(\ell_2 \cos(\theta_2^1) + \ell_3 \cos(\theta_3^1)\right) \tag{7.12}$$

and

$$G_Y^{(2)} = 0 = \frac{2(\Psi_{Y_2} - \Psi_{Y_3})}{(\delta t)^2} - \lambda_Y^{(1)}\frac{1}{M_2} + \lambda_Y^{(2)}\left(\frac{1}{M_2} + \frac{1}{M_3}\right) - \frac{2}{(\delta t)^2}\left(\ell_2 \sin(\theta_2^1) - \ell_3 \sin(\theta_3^1)\right). \tag{7.13}$$

In the next section we discuss our method of solving these equations to get the Lagrange multipliers.

7.2. Solving for the Lagrange multipliers

For the present case where there are three bodies and two links there are six equations $G_n^m = 0$, for the six Lagrange multipliers. Because the equations are non-linear they must be solved using iteration. We tried various forms of point iteration but none converged. We found that either of two forms of the Newton–Raphson converged satisfactorily. The straightforward method was to solve all the equations simultaneously using the Newton–Raphson method. We found that to calculate the Lagrange multipliers with errors $\sim 10^{-10}$ took 3–4 iterations. This represents $\sim 10^{-4}$ of the total CPU time for a single time step.

The disadvantage of this method arises only when there are many bodies and links because the Newton–Raphson equations then become unwieldy. We therefore decided to experiment with another version of Newton–Raphson where we solved link by link then repeated the process i.e. the three Lagrange multiplier equations for link 1 were solved by Newton–Raphson keeping the Lagrange multipliers associated with link 2 fixed. The Lagrange multipliers for link 2 were then found by a Newton–Raphson iteration using the newly calculated Lagrange multipliers for link 1. This procedure was repeated until convergence was achieved. We found it converged to the same accuracy as the previous method but require 100–120 iterations. This represents $\sim 10^{-3}$ of the total CPU time for a single time step.

8. Numerical tests

SPH has been validated against experiment both for rigid bodies dropping vertically into fluids [27] and sliding down a ramp into a fluid [28]. Here, we consider further tests involving one or more bodies. In the following, unless otherwise stated, we use SI units.

8.1. Oscillating cylinders

To show that our algorithm reproduces the correct results for cylinders moving through a fluid we consider two test cases. In the first the cylinder is driven with a simple harmonic motion. In the second the cylinder is tethered to a spring.

8.1.1. A driven cylinder

This problem involves the two-dimensional flow produced by a circular cylinder oscillating in a direction perpendicular to the axis of the cylinder. Dütsch et al. [4] (subsequently referred to as D98) carried out experiments on this system and compared their simulations with the experiments. The experiments were conducted in channels which, for the numerical calculations, were assumed to be at an infinite distance. Other authors have also used this system as a test of numerical methods (see for example [39]) though no simulations agree accurately with the experimental results for the velocity. In particular, the simulations give velocity fields which are symmetric about the direction of oscillation while the experiments show significant departures from that symmetry. In the present tests the channel was replaced by a periodic domain.

We simulated a cylinder of diameter $D = 0.4$ oscillating in the x direction with frequency f according to

$$x = -A\sin 2\pi ft \tag{8.1}$$

with A chosen to give a Keulegan–Carpenter (KC) number

$$\frac{2\pi A}{D} = 5. \tag{8.2}$$

With this value of the KC number the flow is expected to be symmetric about the direction of motion whereas with higher values the flow becomes highly asymmetric (D98). The sound speed was chosen to be 10 times the maximum velocity of the cylinder, $20\pi Af$. The viscosity parameter α is given in terms of the Reynolds number $\Re$ (based on length scale D and the maximum velocity of the cylinder) by

$$\alpha = \frac{112}{150}\left(\frac{D}{h\Re}\right) \tag{8.3}$$

and we take $h = 1.3\Delta p$, where Δp is the initial particle spacing. The value of α therefore depends on the resolution and $\Re$. In the calculations described here $\Delta p = 0.02$ and $\Re = 100$.

The fluid particles were initially placed on a grid of squares of side Δp within a periodic cell of size 2×2. The forces on the particles depend on both the particles in the cell and the particles in the neighbouring cells of the periodic array. Only those neighbouring particles which can interact with those in the cell need be retained.

Particles within a radial distance of approximately $(D/2 + h)$ from the centre of the cylinder were omitted. The mass of each particle is $\rho(0)(\Delta p)^2$ where $\rho(0) = 1.02\rho_0$ is the initial density of the fluid and ρ_0 is the reference density used in the equation of state. This means that the background pressure is non-zero. The system was then damped for a time 1.76s or 3000 steps to enable the SPH liquid particles to come into equilibrium with the boundary forces from the cylinder. During this time the cylinder was kept fixed. After the damping the oscillation of the cylinder began.

For a given boundary of the body or bodies, in this case a circle with radius 0.2, we need to determine where the boundary particles should be placed to give the best approximation to the flow. Because the boundary particles exert a repulsive force on the fluid particles we expect the boundary particles should be placed on a circle with radius slightly less than the specified radius of the cylinder. We considered an inward shift of the radius of $\frac{1}{2}\Delta p, \Delta p$ and $\frac{3}{2}\Delta p$ and from these values estimated the choice of shift for minimum error in the drag force.

Fig. 2 shows the velocity field at phase 3π (radians). There are no detailed results with which to compare the overall velocity field but it is in good qualitative agreement with the streamlines in Fig. 7 of D98. Fig. 3 shows the total drag and viscous forces for the SPH simulation with initial particle spacing $\sim$0.02 using approximately 10,000 particles. The boundary particles are on a circle of radius $R = \frac{1}{2}(D - \Delta p)$. The agreement of the viscous force with that calculated by D98 is very good, and the total drag force is satisfactory with some oscillations at the peak values. The SPH results are comparable to the numerical results of Wan and Turek who use 32,768 grid points and a moving mesh. The mean square error and the absolute error (measured from those of Dütsch) are given for the shifts of radius of the particles from the actual radius in Table 1. The minimum is obtained when the circle on which the particles are placed is inside the actual boundary by $\frac{1}{2}\Delta p$.

In summary these results show that, at the resolutions we have considered where $\Delta p = 0.02$ and therefore 63 particles around the circumference of the cylinder, the drag forces on the cylinder are calculated with satisfactory accuracy (comparable to that of D98 with 192 points around the circumference, and with that of Wan and Turek using 32,768 points with variable resolution and a moving mesh, but in a domain which is four times larger than used here, but less accurate than in the immersed boundary method of Kim and Choi [13] who used 68,129 points with higher resolution near the body).

8.1.2. Flow past a tethered cylinder

The problem of the oscillation of a cylinder tethered by an elastic spring and submerged in a stream of fluid is important for many industrial problems. Vortices are periodically cast off the cylinder and resonate with the cross channel oscillations. Here, we simulate the two dimensional version of this problem studied by Nomura and Hughes [31]. They used an arbitrary Lagrangian–Eulerian finite element technique with a much finer resolution near the cylinder (of diameter D) which was placed in a channel of length $24D$ and width $12D$ with the elastic force directed perpendicularly to the axis of the channel. The ratio of the mass of the cylinder to an equal volume of the streaming fluid was 3.0, and the dimensionless quantity $V/(Df)$, where V is the upstream velocity and f is the oscillation frequency of the spring equal to 7.1. In the results reported here the lengths are scaled using D and the velocity scaled using V.

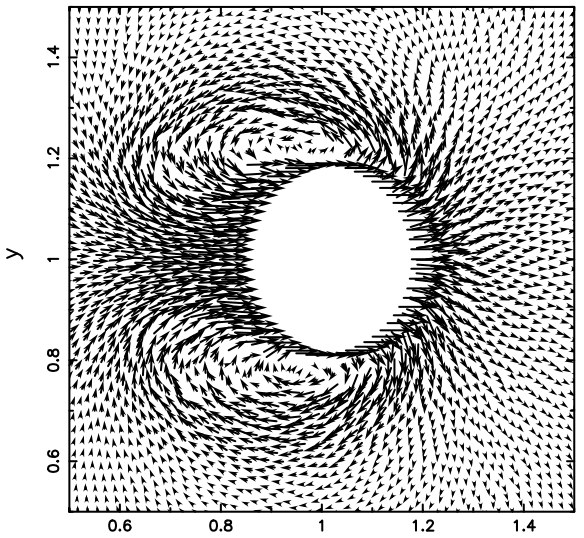

Fig. 2. The velocities of the SPH particles at phase 3π after $t = 0$. The centre of the cylinder (circle) was initially at $x = 1.0$, $y = 1$. The velocity arrows for a particle start on the particle. Note the symmetric vortices produced by the flow in agreement with the results of D98.

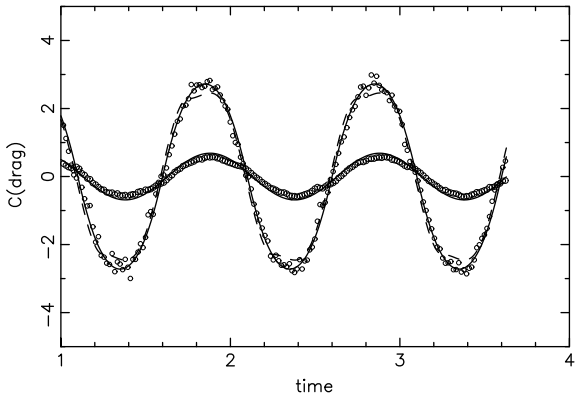

Fig. 3. The total drag force measured by D98, is shown by the continuous line and the drag formula of D98 is shown by the dashed line. The smaller amplitude curve shows the viscous force. The SPH results are shown by small circles. The SPH results for the total force show oscillations at the peak values but give a better estimate of the drag force than the drag formula of D98. The agreement for the viscous forces is very good.

Table 1
Table showing the mean square error and the absolute error for the drag force for various inward shifts in the radius of the circle on which the boundary particles were placed

Sq-error	Abs-error	Shift/Δp
0.105	0.073	0.0
0.091	0.059	0.5
0.107	0.075	1.0
0.142	0.105	1.5

In our simulation we represented the channel walls by boundary particles and injected fluid particles with a constant density and velocity equal to the upstream velocity. The outflow condition was approximated by allowing the particles to have free flow at the end of the channel and allowing this free flow to continue for a further $4h$. Particles which flowed out of this region were eliminated from the list of particles. As in the previous example the liquid particles were placed on a grid of squares rejecting those inside a circle centred on the cylinder and with radius=$\frac{1}{2}D + \Delta p$. The centre of the cylinder was displaced $0.2D$ in the direction of the spring restoring force as in Case 3 of Nomura and Hughes [31]. The liquid SPH particles were damped for 2500 steps so that the liquid particles could come into equilibrium with the boundary forces.

During the damping the cylinder was held fixed. The Reynolds number of the flow was 200 and 120×240 liquid SPH particles were used with an initial particle spacing of 0.1.

In Fig. 4 we show the vorticity calculated a distance $6D$ downstream of the cylinder. The alternate peaks of positive and negative vorticity show up clearly. The Strouhal number is 0.16. This is lower than that for a cylinder in an effectively infinite fluid for which the Strouhal number is 0.18 [8], but larger than that of Nomura and Hughes who obtained the value 0.14. Our results are consistent with those of Chen et al. [2, pp. 36–37] who show that a channel of width $5D$ the Strouhal number is 0.17.

In Fig. 5 we show the amplitude as a function of time. In the initial stage the amplitude of $0.2D$ drops to a very low value as the flow around the cylinder adjusts to the sudden change of the fluid velocity after the damping. Eventually the vortices from the flow around the cylinder initiate strong oscillations of the body. The amplitude of these oscillations varies, but the average is very close to the average of those found by Nomura and Hughes [31] which is $\sim 0.2D$.

8.2. The motion of three linked bodies

We now consider a set of tests involving the motion of three identical linked bodies. In the first of these we simulate three linked diamonds in a symmetric flapping motion and show that the integration faithfully maintains the symmetry and the calculation converges as the resolution is increased. The second test is a viscous version of the simulation of K05. The third test shows that our method, without any changes to the algorithm, handles linked bodies swimming through a surface.

8.2.1. Flapping diamonds

We now consider the flapping gait of three identical linked diamonds. The diamonds (rhombs) have side length 0.3, and acute angle $\pi/3$. The links are a distance 0.075 from the points at the ends of the long diameter of the diamonds. We place the diamonds in a periodic 3×3 box with the centre of mass of the central body in the centre of the box. The initial angles θ_k are all initially zero and the gait is determined by $\varphi_1 = 0.125(1 - \cos(\omega t))$ and $\varphi_2 = 0.125(1 - \cos(\omega t))$. The initial linear and

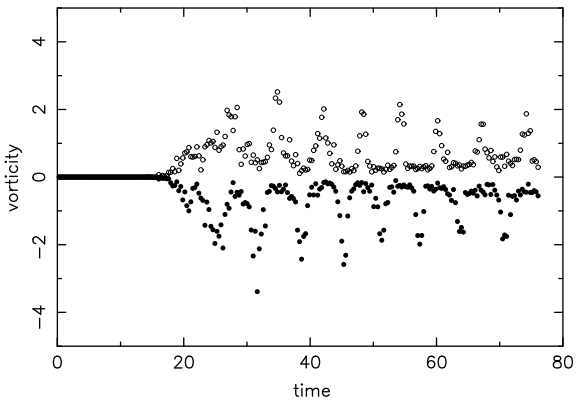

Fig. 4. The vorticity downstream of a cylinder in a channel. The cylinder was tethered by a spring to the centre of the channel. The filled circles show negative vorticity and the open circles show positive vorticity.

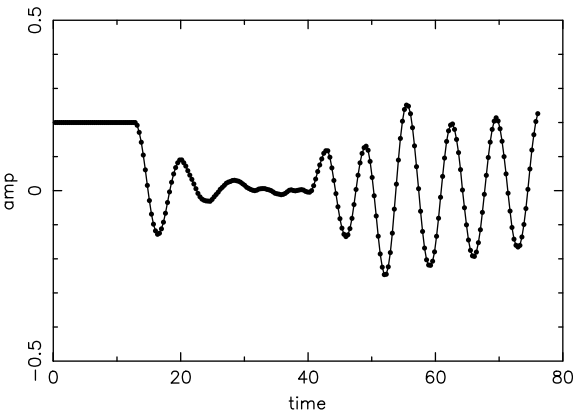

Fig. 5. The amplitude of the oscillations of the tethered cylinder.

angular momentum of each of the bodies are zero consistent with the constraints and the symmetry. The density of the bodies is the reference density ρ_0 of the fluid, which we assume is that of pure water 1000 kg/m^3. We set the initial density of the water as $1.02\rho_0$ as in Section 8.1.1.

We take the speed of sound $c_s = 10 \times (\omega d)$ where we have estimated a typical fluid velocity as ωd. In the present calculations $\omega = 1$. For the results shown here the parameter α in the viscosity was 0.05. Referring to (3.4) the Reynolds number is

$$\Re = \frac{112VL}{15\alpha h v_{\mathrm{sig}}}, \tag{8.4}$$

where V is a characteristic velocity and L is a characteristic length. We take $V = 0.1c_s = d\omega$, and the long diameter of the diamond as L. The signal speed $v_{\mathrm{sig}} \simeq c_s$. When the particle spacing $\Delta p = 0.025$ and $h = 1.3\Delta p$ then the Reynolds number is approximately 240.

Because of the symmetry of the configuration $X_1 = X_3$, $Y_1 = Y_3$, $\theta_1 = -\theta_2$. The symmetry also requires that the Lagrange multipliers satisfy the condition $\left[\lambda_X^{(1)} = \lambda_X^{(2)}, \lambda_Y^{(1)} = \lambda_Y^{(1)} \text{ and } \lambda_\theta^{(1)} = -\lambda_\theta^{(2)}\right]$.

The fluid particles were initially placed on a grid of square cells as described earlier for the oscillating cylinder. Particles within approximately h of the boundary of the diamonds were omitted. The system was then damped for $\sim$7 s. During the damping the diamonds were held fixed. After this time the diamonds move with the specified gait.

Fig. 6 shows the particle configuration of the central body and the velocity field 4200 steps after the damping has finished. The particle spacing is 1/60, and there are approximately 21,000 particles. The particles maintain the symmetry to high accuracy as can be seen by checking the velocity vectors on the left and right sides of the central body. At time equivalent to 5000 steps, or two body oscillation periods after the damping, the Lagrange multipliers satisfy the symmetry conditions given above to 1 part in 10^7, and the symmetry conditions on the centre of mass coordinates of the bodies are maintained to at least 1 part in 10^5. The linear momentum was conserved to round off error. As mentioned earlier the angular momentum is not conserved to round off error. However, in this case, because of the symmetry, the angular momentum was conserved to 1 part in 10^8.

In order to estimate the convergence we ran the simulation with initial particle spacings of 1/20, 1/30, 1/40 and 1/60. We show in Fig. 7 the y component of the velocity of the central body against time. We found there were slight constant phase shift differences when the resolution was changed and, to estimate the effective amplitude errors, the results for all resolutions apart from 1/60 were shifted in time. As an example the phase shift for resolution 1/40 was approximately 3% of the period. This figure shows that the calculation with resolution 1/40 tracks that with resolution 1/60 closely with maximum errors at the peaks and valleys.

If the mean square error in the velocity varies with particle spacing according to βh^p then we can estimate p by comparing the results for spacings 1/30 and 1/40 with those for 1/60. We calculate

$$\epsilon_1 = \sqrt{\frac{1}{r}\sum_{i=1}^{r}(v_{30,i} - v_{60,i})^2}, \tag{8.5}$$

where for example, $v_{30,i}$ denotes the ith value of the y component of the velocity of body 2 with spacing 1/30, and we calculate

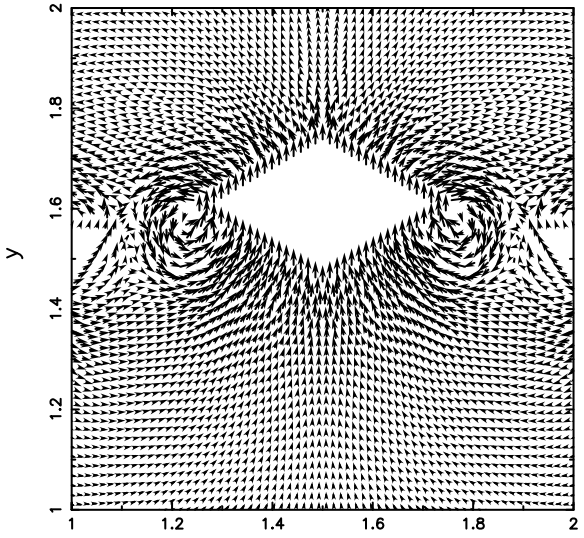

Fig. 6. The velocities of the SPH particles as the central body begins to move up. Note the excellent symmetry maintained by the particles, and the vortices produced at the tips of the diamonds.

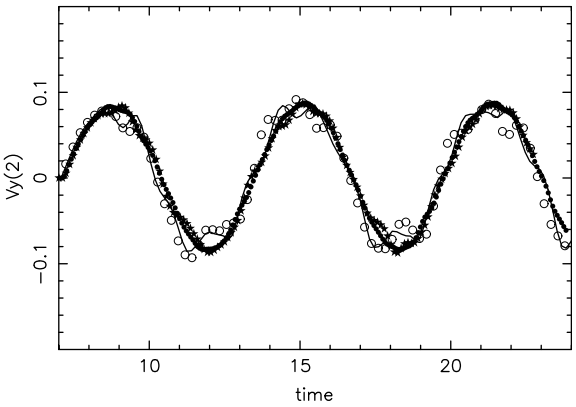

Fig. 7. The y component of the velocity of the body 2, the central body, against time for different resolutions. The results for particle spacing 1/20 are shown by open circles, for spacing 1/30 by the continuous line, for spacing 1/40 by dark stars, and 1/60 by filled small circles. Note that the results for spacing 1/40 track those for 1/60 closely while the results for spacing 1/20 and 1/30 show large variations, especially near the peaks.

$$\epsilon_2 = \sqrt{\frac{1}{r}\sum_{i=1}^{r}(v_{40,i} - v_{60i})^2}. \tag{8.6}$$

In order to calculate these summations we interpolated the velocities to 200 equi-spaced points in the range $8 \leqslant t \leqslant 22$. The ratio ϵ_1/ϵ_2 can be written in terms of the error according to

$$\frac{\epsilon_1}{\epsilon_2} = \frac{\left(\frac{1}{30}\right)^p - \left(\frac{1}{60}\right)^p}{\left(\frac{1}{40}\right)^p - \left(\frac{1}{60}\right)^p}. \tag{8.7}$$

The solution of this equation gives $p \simeq 1.9$ so that the convergence is nearly second-order.

In summary, the simulated flapping motion of the diamonds preserves the symmetry very accurately and, with the parameters of the bodies and the periodic box we have used, a particle spacing of 1/40 gives a close approximation to that with 1/60. The convergence of the velocity of the central body is nearly quadratic in h.

8.2.2. The motion of three linked ellipses

We now describe the motion of three linked, identical ellipses moving in a fluid in two dimensions. As mentioned earlier, this system was considered by K05 for inviscid fluids and for both massless and neutrally buoyant bodies, and by Eldredge [6] for a viscous fluid and massless bodies. K05 studied both forward and turning gaits, whereas Eldredge considered only the forward gait. These authors assumed the fluid to be infinite in extent. In this paper we compute the motion with the forward gait for neutrally buoyant bodies, and we use a periodic domain for the fluid.

The ellipses we consider have semi-major axis $a = 2/9$, semi-minor axis $b = 0.2a$, and distance from the end of the major axis to the link or pivot point $c = 0.2a$. For the reasons discussed in the previous section, we place the boundary particles on an ellipse of semi-major axis $a^* = a - 0.5\Delta p$ and semi-minor axis $b^* = a - 0.5\Delta p$, where Δp is the initial particle spacing. Hence the distance between the tip of the ellipse formed by the boundary particles and the link is $c^* = c + 0.5\Delta p$. The ellipses had mass $M = \rho_0 \pi ab$ and moment of inertia $I = M(a^2 + b^2)/4$. The actual density of the fluid was set to $1.02\rho_0$ as in the case of flapping diamonds. The boundary particles on the ellipse can be placed as desired. For example they could be closer together in regions of small radius of curvature to delineate the boundary more accurately. However, for the present simulation we chose to make the boundary particle spacing the same as the liquid particle spacing Δp. The fluid particles were placed on a grid of square cells inside a cell of side $18a$ using periodic boundary conditions. Particles closer to the ellipses than a distance of $\sim h$ were omitted. For the calculations to follow the initial fluid particle spacing was $\Delta p = 0.025$ and $h = 1.3\Delta p$. As in the previous simulations the bodies were held in a fixed position while the fluid SPH particles were allowed to come to equilibrium.

The forward gait of motion was specified by setting $\varphi_1 = \cos(\omega t)$ and $\varphi_2 = \sin(\omega t)$ (see K05 but note that our notation differs from theirs). We take the speed of sound c_s to be $20a\omega$ and the signal velocity $v_{sig} \simeq c_s$. In our simulations we take ω to be 1. We define a Reynolds number $\mathfrak{R}$ by taking the characteristic velocity $v_{typ} = 2a\omega$ and the characteristic length scale as $2a$ so that

$$\mathfrak{R} = \frac{\omega(2a)^2}{\nu} = \frac{112}{75\alpha}\frac{a}{h}. \tag{8.8}$$

We chose the initial velocities to be such that the initial linear and total angular momentum are zero (see Appendix A). The initial velocities for this case are given in Table 2 and are independent of the size of the domain, and the viscosity. The initial linear and angular velocities for the simulations of K05 and Eldredge [5] are not available. The initial coordinates of the centre of mass of the central body were $(X_2, Y_2) = (x_c - 0.5/\sqrt{2}, y_c + 0.5/\sqrt{2})$, where x_c and y_c are the coordinates of the centre of the box. The initial values of the angles were $\theta_1 = -1$ and $\theta_2 = \theta_3 = 0$.

Our results for all viscosities and for a range of a/b from 2 to 10 are in qualitative agreement with the calculations of K05 and Eldredge [5] which are characterised by a zig-zag motion of the centre of mass of the middle body as shown in Fig. 8 for the case $a/b = 5$. The results differ in detail because K05 assume the flow is inviscid their strides are longer than we (and Eldredge) get with non-zero viscosity. Our results also differ to those of Eldredge because he considers massless bodies, and the distance from the tips of the ellipses to the link (pivot point) relative to the major axis of the ellipses in his calculations is different from that of K05.

The stride length is defined as the distance between successive turning points in the same sense i.e. down then up (which defines the lower set of turning points), or up then down (which defines the upper set of turning points). Fig. 8 shows that the stride length is smaller when the viscosity is higher (larger α, smaller $\mathfrak{R}$) and that the loops at the turning points of the trajectory are larger when the viscosity is higher. We found that the stride length, for a given viscosity, would vary from stride to stride. The variance is $\sim$10% with $\alpha = 0.05$, reducing to $\sim$4% with $\alpha = 0.002$. A thorough exploration of the reason for this variation, including a study of the influence of the viscosity, periodic boundaries and the resolution, will be presented elsewhere.

8.2.3. Swimming through a free surface

As a final test of the convergence with resolution, and as an example of the flexibility of our method, we consider linked bodies swimming out of a potential field and through a free surface. The fluid was held in an axisymmetric potential well with a force proportional to $\mathbf{r}$, where $\mathbf{r}$ is a radial vector from the origin. The linked bodies also feel this force, but if it is not too strong, they are able to swim out of the fluid and through the free surface. This setup also allows us to test angular momentum conservation under circumstances when it should be conserved exactly. Fig. 9 shows the configuration as the bodies swim through the surface.

The linked bodies were set up the same way as described in Section 8.2.2. The fluid occupied a circular area of radius 1.5 and the centre of body 2 was initially at the origin. The external force/mass was taken as $-0.1/\mathbf{r}$. With a particle spacing of 0.05, $\mathfrak{R}$ was approximately 150.

We ran the simulation for initial particle spacings of 1/20, 1/30, 1/40 and 1/50 to calculate how the path followed by the linked bodies converges with resolution. Fig. 10 illustrates the paths and shows that the differences increase as the bodies swim closer to the surface. The path for $\Delta p = 1/50$ was used as a reference and the distances between the first upper peak and that for the other resolutions were measured (shown by the open circles in Fig. 11). Similarly, the distances for the second peak were measured and shown by the open square symbols in Fig. 11. The distances between the peak for 1/50 and another resolution gives an estimate of the error, ε. Fig. 11 also shows that the error is proportional to $\varepsilon \propto (\Delta p)^2$. The configuration of the bodies and the fluid when the bodies are close to the surface is illustrated in Fig. 12. This figure shows that the state of the

Table 2
The initial velocities for the forward gait

Body	1	2	3
Ω	-2.771×10^{-1}	-2.771×10^{-1}	7.229×10^{-1}
$\dot{X}$	-4.146×10^{-2}	2.073×10^{-2}	2.073×10^{-2}
$\dot{Y}$	-3.626×10^{-2}	7.757×10^{-2}	-4.131×10^{-2}

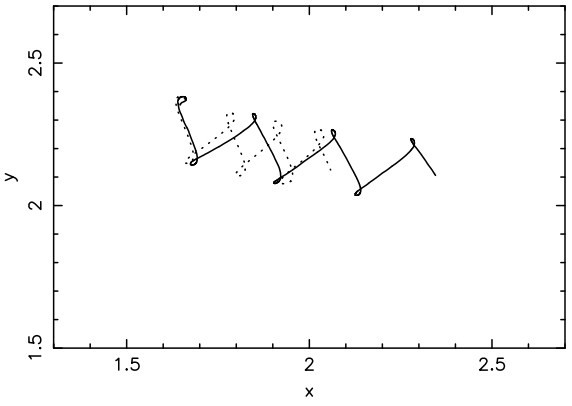

Fig. 8. The path of the centre of mass of body 2 for the forward gait with $a/b = 5$. The solid line indicates the path for $\alpha = 0.002$ or Reynolds number $\mathfrak{R} \simeq 5100$. The dotted line is for $\alpha = 0.05$ or $\mathfrak{R} \simeq 200$. The stride length increases as $\mathfrak{R}$ increases, and the size of the loops at the peaks of the zig-zags increase as $\mathfrak{R}$ decreases.

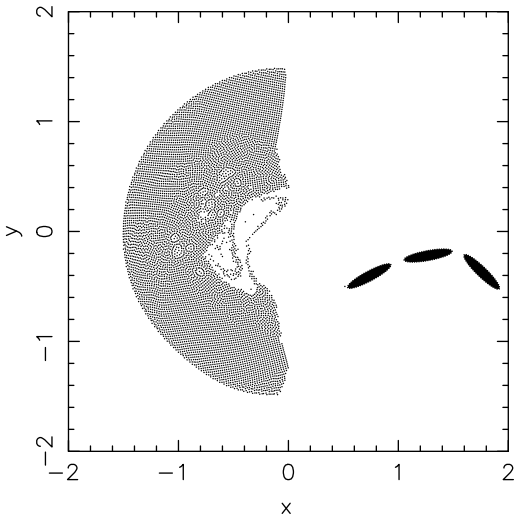
2
1
0
−1
−2
y
−2
−1
0
1
2
x

fluid near the exit point of the first body is sensitively dependent on the resolution while the position of the bodies is much less sensitive.

As mentioned previously, we expect the angular momentum to be well conserved in this test. We find that the angular momentum is conserved to ~ 1 part in 10^6 and the error is $\propto(\delta t)^2$ showing that it is due to the fact that the constraint conditions are satisfied at the mid-point of the step and not at the end of the step as discussed in Section 5.

9. Conclusions

We have derived an SPH formulation of the problem of swimming linked bodies and applied it to the motion of three linked bodies. Constraints associated with the linkage of the bodies, and the specification of the time variation of the orientation angles of the bodies, have been included by using Lagrange multipliers which can be calculated efficiently using either of two versions of the Newton–Raphson method. Boundaries were treated using boundary particles in a manner similar to the immersed boundary method of Peskin [32,33] with the optimum positions of the particles being determined from the drag on an oscillating cylinder. The form of the boundary force ensures linear and angular momentum are conserved by these forces. The time stepping algorithm we use is similar to the symplectic Verlet integrator. In the absence of dissipation it is reversible and conserves linear momentum exactly, but the conservation of angular momentum is not exact both because of the periodic boundaries and because the constraints are satisfied at the end point of a step rather than at the mid-point. The details are discussed in the text.

The method was first tested by calculating the drag on a cylinder with a specified oscillation, and the dynamics of a cylinder tethered to a spring in a stream of fluid flowing through a channel. The agreement with other calculations and experiments, where available, is good. The second set of experiments involved three linked bodies. The first of these involved the flapping mode of three linked diamonds in periodic domain. The results showed that the conservation of symmetry, linear and angular momentum was excellent. A convergence study showed close to quadratic convergence. The second experiment involved three linked ellipses in a forward gait within a periodic domain. The results were in qualitative agreement with those of K05 in an infinite inviscid fluid, and Eldredge [6] for massless bodies in an infinite viscous fluid. The final test involved three linked ellipses swimming in a fluid with a free surface subject to a radial force. This test showed that our method is able to handle a free surface without difficulty. Convergence of the motion with resolution was found to be quadratic although the coefficient becomes larger as the bodies approach the surface.

The formulation we have used is general and can be immediately applied to the motion of linked bodies in stratified fluids, or with a free surface, or within complex boundaries, or with more complex constraints including those where the gait depends on the positions of the bodies in the domain. The extension to three dimensions is straightforward. The further extension to bodies covered by an elastic material is also straightforward and has applications to biological problems.

Appendix A. The initial conditions

In this paper, we choose initial conditions where the linear momentum of the linked bodies is zero and the total angular momentum about the centre of mass is zero. These conditions can be reduced to three equations which specify the initial linear velocities and angular velocity of body 1.

For completeness we give the essential details. First, from the derivative with respect to time of the constraint conditions

so that

$$\Omega_{k+1} = \Omega_1 + (\dot{\varphi}_1 + \dot{\varphi}_2 + \dot{\varphi}_3 + \cdots + \dot{\varphi}_k). \tag{A.2}$$

In the same way the constraints on the X_k and the Y_k can be differentiated and for $k > 1$ each $\dot{X}_k$ can be written in terms of X_1 and $\dot{\Omega}_1$ and $\dot{Y}_k$ can be written in terms of $\dot{Y}_1$ and $\dot{\Omega}_1$. The condition that the total X component of momentum of the bodies is zero in the case of three bodies can be written

$$(M_1 + M_2 + M_3)\dot{X}_1 + A\Omega_1 + B = 0, \tag{A.3}$$

where (with $s_k = \sin\theta_k$ and $c_k = \cos\theta_k$)

$$A = M_2(\ell_1 s_1 + \ell_2 s_2) + M_3(\ell_1 s_1 + 2\ell_2 s_2 + \ell_3 s_3) \tag{A.4}$$

and

$$B = M_2(\ell_2 s_2 \dot{\varphi}_1) + M_3(2\ell_2 s_2 \dot{\varphi}_1 + \ell_3 s_3(\dot{\varphi}_1 + \dot{\varphi}_2)). \tag{A.5}$$

In the same way the condition that the Y component of momentum vanishes reduces to

$$(M_1 + M_2 + M_3)\dot{Y}_1 - D\Omega_1 - E = 0, \tag{A.6}$$

where

$$D = M_2(\ell_1 c_1 + \ell_2 c_2) + M_3(\ell_1 c_1 + 2\ell_2 c_2 + \ell_3 c_3) \tag{A.7}$$

and

$$E = M_2(\ell_2 c_2 \dot{\varphi}_1) + M_3(2\ell_2 c_2 \dot{\varphi}_1 + \ell_3 c_3(\dot{\varphi}_1 + \dot{\varphi}_2)). \tag{A.8}$$

The angular momentum consists of the spin angular momentum and the angular momentum of the centre of mass of each body about a fixed point which we choose as the centre of mass of the system of rigid bodies. With the same notation as before, and denoting coordinates taken with respect to the centre of mass of the system by $\overline{X}$ and $\overline{Y}$, the expression for the total angular momentum becomes to

$$\Omega_1 H = G, \tag{A.9}$$

where

$$H = I_1 + I_2 + I_3 - M_2(\overline{X}_2(\ell_1 c_1 + \ell_2 c_2) + \overline{Y}_2(\ell_1 s_1 + \ell_2 s_2)) - M_3(\overline{X}_3(\ell_1 c_1 + 2\ell_2 c_2 + \ell_3 c_3) + \overline{Y}_3(2\ell_2 s_2 + \ell_3 s_3)) \tag{A.10}$$

and

$$G = -I_2\dot{\varphi}_1 - I_3(\dot{\varphi}_1 + \dot{\varphi}_2) + M_2\dot{\varphi}_1(\overline{X}_2\ell_2 c_2 + \overline{Y}_2\ell_2 s_2) + M_3(\overline{X}_3(2\ell_2 c_2\dot{\varphi}_1 + \ell_3 c_3(\dot{\varphi}_1 + \dot{\varphi}_2)) + \overline{Y}_3(2\ell_2 s_2\dot{\varphi}_1 + \ell_3 s_3(\dot{\varphi}_1 + \dot{\varphi}_2))). \tag{A.11}$$

Once Ω_1 is calculated from (A.9), $\dot{X}_1$ and $\dot{Y}_1$ can be calculated from (A.3) and (A.6) after which $\dot{X}_2, \dot{Y}_2, \dot{X}_3, \dot{Y}_3, \Omega_2$ and Ω_3 can be calculated from the derivatives of the constraints.

References

[1] J. Carling, T.L. Williams, G. Bowtell, Self-propelled anguilliform swimming: simultaneous solution of the two-dimensional Navier–Stokes equations and Newton's laws of motion, J. Exp. Biol. 201 (1998) 3143–3166.
[2] J.-H. Chen, W.G. Pritchard, S.J. Tavener, Bifurcation for flow past a cylinder between parallel planes, J. Fluid Mech. 284 (1995) 23–41.
[3] S. Childress, Mechanics of Swimming and Flying, Cambridge University Press, London, 1981.
[4] H. Dütsch, F. Durst, S. Becker, H. Lienhart, Low-Reynolds-number flow around an oscillating circular cylinder at Low Keulegan–Carpenter numbers, J. Fluid Mech. 360 (1998) 249–271.
[5] J.D. Eldredge, Numerical simulations of undulatory swimming at moderate Reynolds number, Bioinsp. Biomimet. 1 (2006) S19–S24.
[6] J.D. Eldredge, Numerical simulation of the fluid dynamics of 2D rigid body motion with the vortex particle method, J. Comput. Phys. 221 (2007) 626–648.
[7] L.J. Fauci, C.S. Peskin, A computational model of aquatic animal locomotion, J. Comput. Phys. 77 (1988) 85–108.
[8] U. Fey, M. Konig, H. Eckelmann, A new Strouhal–Reynolds number relationship for the circular cylinder in the range $47 < R_e < 3 \times 10^5$, Phys. Fluids 10 (1998) 1547–1549.
[9] Sir James Gray, Animal Locomotion, Weidenfeld and Nicholson, London, 1968.
[10] J. Gray, J.J. Monaghan, R. Swift, SPH elastic dynamics, Comput. Method Appl. Mech. Eng. 190 (2001) 6641–6662.
[11] G.J. Hancock, The self-propulsion of microscopic organisms through liquids, Proc. R. Soc. 217 (1953) 96–121.
[12] E. Kanso, J.E. Marsden, C.W. Rowley, J.B. Melli-Huber, Locomotion of articulated bodies in a perfect fluid, J. Nonlinear Sci. 15 (2005) 255–289 (referred to in the text as K05).
[13] D. Kim, Haecheon Choi, Immersed boundary method for flow around and arbitrarily moving body, J. Comput. Phys. 212 (2006) 662–680.
[14] H. Lamb, Hydrodynamics, sixth ed., Cambridge University Press, 1932.
[15] L.D. Landau, E.M. Lifshitz, Mechanics: Course of Theoretical Physics, Vol I. Mechanics, Pergamon, 1976.
[16] B.J. Leimkuhler, R.D. Skeel, Symplectic numerical integrators in constrained Hamiltonian systems, J. Comput. Phys. 112 (1994) 117–125.
[17] M.J. Lighthill, Mathematical Biofluiddynamics, SIAM, Philadelphia, 1975.
[18] M.J. Lighthill, Flagellar hydrodynamics, SIAM Rev. 18 (1976) 161–230.
[19] M.J. Lighthill, in: Hussaini My (Ed.), Collected Papers of Sir James Lighthill, Oxford University Press, 1997.
[20] H. Liu, R. Wassersug, K. Kawachi, A computational fluid dynamics study of tadpole swimming, J. Exp. Biol. 199 (1996) 1245–1260.

[21] H. Liu, R. Wassersug, K. Kawachi, The three-dimensional hydrodynamics of tadpole locomotion, J. Exp. Biol. 200 (1997) 2807–2819.
[22] J.B. Melli, C.W. Rowley, D.S. Rufat, Motion planning for an articulated body in a perfect planar fluid, SIAM J. Appl. Dyn. Syst. 5 (4) (2006) 650–669.
[23] J.J. Monaghan, Smoothed particle hydrodynamics, Ann. Rev. Astron. Astro. 30 (1992) 543–573.
[24] J.J. Monaghan, Simulating free surface flows with SPH, J. Comput. Phys. 110 (1994) 399–406.
[25] J.J. Monaghan, SPH and Riemann solvers, J. Comput. Phys. 136 (1997) 298–307.
[26] J.J. Monaghan, SPH without a tensile instability, J. Comput. Phys. 159 (2000) 290–311.
[27] J.J. Monaghan, A. Kos, Scott Russells wave generator, Phys. Fluids A 12 (2000) 622–630.
[28] J.J. Monaghan, A.M. Kos, N. Issa, Fluid motion generated by impact, J. Waterways Ports Coast. Ocean. Eng. 129 (6) (2003) 250–259.
[29] J.J. Monaghan, Smoothed particle hydrodynamics, Rep. Progress Phys. 68 (2005) 1703–1759.
[30] J.J. Monaghan, Smoothed particle hydrodynamics simulations of shear flow, Mon. Not. R. Astro. Soc. 365 (2006) 199–213.
[31] Takashi Nomura, T.J.R. Hughes, An arbitrary Lagrangian–Eulerian finite element method for the interaction of fluid and rigid body, Comput. Method Appl. Mech. Eng. 95 (1992) 115–138.
[32] C.S. Peskin, Numerical analysis of blood flow in the heart, J. Comput. Phys. 25 (1977) 220.
[33] C.S. Peskin, The immersed boundary method, Acta Numer. 10 (2002) 479–517.
[34] E.M. Purcell, Life at low Reynolds number, Am. J. Phys. 45 (1977) 3–11.
[35] M. Sfakiotakis, D.M. Lane, J. Davies, C. Bruce, Review of Fish Swimming modes for Aquatic locomotion, IEEE J. Ocean. Eng. 24 (2) (1999) 237–252.
[36] G.I. Taylor, The action of waving cylindrical tails in propelling microscopic organisms, Proc. R. Soc. A. 211 (1952) 225–239.
[37] M.S. Triantafyllou, G.S. Triantafyllou, D.K.P. Yue, Hydrodynamics of fishlike swimming, Ann. Rev. Fluid Mech. 32 (2000) 33–53.
[38] E.D. Tytell, G.V. Lauder, The hydrodynamics of eel swimming I Wake structure, J. Exp. Biol. 207 (2004) 1825–1841.
[39] Decheng Wan, Stefan Turek, Fictitious boundary and moving mesh methods for the numerical simulation of rigid particulate flows, J. Comput. Phys. 222 (2007) 28–56.
[40] M.J. Wolfgang, J.M. Anderson, M.A. Gorsenbaugh, D.K. Yue, M.S. Triantafyllou, Near-body flow dynamics in swimming fish, J. Exp. Biol. 202 (1999) 2303–2327.